Journal of Power Sources 195 (2010) 5155–5166

Contents lists available at ScienceDirect

Journal of Power Sources

journal homepage: www.elsevier.com/locate/jpowsour

Investigation of sheet resistance in thin-film mixed-conducting solid oxide fuel cell cathode test cells

Matthew E. Lynch, Meilin Liu*

Center for Innovative Fuel Cell and Battery Technologies, School of Materials Science and Engineering, Georgia Institute of Technology, 771 Ferst Dr., Atlanta, GA 30332, USA

ARTICLE INFO

Article history:
Received 20 December 2009
Received in revised form 8 March 2010
Accepted 8 March 2010
Available online 15 March 2010

Keywords:
Solid oxide fuel cell
Modeling
Test cell
Thin-film
Mixed ionic-electronic conductor
Sheet resistance

ABSTRACT

Patterned and thin-film electrode experiments are effective in isolating or separating the complex charge and mass transport processes involved in the oxygen reduction reaction within and on the surface of a mixed-conducting solid oxide fuel cell cathode, making it possible to correlate electrochemical performance with electrode geometry, reaction pathway, and limiting steps. Very little information about either the impact of sheet resistance on global response or on effective design of current collector configuration to avoid sheet resistance has been reported to date, however. In this contribution, an empirical numerical model is presented to simulate sheet resistance under various material and catalytic parameters, current collector configurations, and other experimental factors in thin-film, mixed-conducting working electrodes. This model is used to provide general guidance for effective current collector placement by mapping in parameter space. In general, continuous crisscrossing metal lines, deposited through e.g. photolithography, provide the best intra-film current collection while small, regularly spaced discrete contacts, provided by e.g. a metal mesh, provide less efficient intra-film current collection. Most thin-film aspect ratios and current collector configurations can be accommodated without severe intra-film sheet resistance limitation provided the current collectors are spaced appropriately.

1. Introduction

The oxygen reduction kinetics associated with porous solid oxide fuel cell (SOFC) cathodes are difficult to fully characterize. This difficulty is largely due to the fact that the constituent materials are, to one degree or another, mixed ionic-electronic conductors (MIECs). Simplified thin-film test cell geometries have been used recently to isolate and investigate various kinetic/catalytic properties of the materials [1–27]. The purpose of this paper is to provide guidance on the design of such test cells with respect to the phenomenon of sheet resistance and the placement of current collectors (CCs) in the cells.

Test cells consist of thin films of SOFC cathode materials deposited onto single-crystal or finely polished polycrystalline electrolyte substrates via physical vapor deposition into continuous, unbroken layers or into patterns defined by photolithography. Metallic CCs on the surface of the working electrode provide electrical connection for electrochemical impedance spectroscopy (EIS) measurements. A low-impedance porous layer on the opposite side of the electrolyte substrate often serves as a counter electrode.

One problem with this setup is sheet resistance in the thin-film working electrode. The local electrical potential within the MIEC can vary from its value at the CC, resulting in nonuniform electrochemical kinetics across the surface of a test cell. Since typical test cells measure macroscopic electrochemical response, the nonuniform response is buried within the cell measurement, convoluting geometric effects with intrinsic material properties and leaving some uncertainty about the true catalytic properties. The effect of sheet resistance is more severe when thinner films and larger CC spacings are used.

Sheet resistance has been observed in experimental SOFC work [2,16,21] and in models tailored to $La_{1-x}Sr_xMnO_{3\pm\delta}$ (LSM) test cells [28,29]. The region in a solid electrolyte around an electrode has been investigated numerically [30–33] and there have been a few studies that address sheet resistance within metallic thin-film working electrodes [34–36]. However, mixed conduction, a solid electrolyte, and SOFC cell kinetics greatly complicate the issue.

The test cell comprised of a thin-film mixed conductor on a solid electrolyte has a singular set of challenges associated with it that set it apart from related electrochemical systems, such as fuel cell stacks and batteries, and the current collection analysis associated with them. The extreme aspect ratios of the thin-film and the low conductivity compared to metals make the working electrode particularly susceptible to deactivation by sheet resistance. Changing the film thickness may alter not only the conductance, but also the

* Corresponding author. Tel.: +1 404 894 6114; fax: +1 404 894 9140.
E-mail addresses: matt.lynch@gatech.edu (M.E. Lynch), meilin.liu@mse.gatech.edu (M. Liu).

0378-7753/$ – see front matter © 2010 Elsevier B.V. All rights reserved.
doi:10.1016/j.jpowsour.2010.03.017

Nomenclature

List of symbols

B_B^x	occupied B lattice site
$B_B^{\cdot}$	positively charged B-site small polaron, bound electron hole
B_B'	negatively charged B-site small polaron, bound electron
e^-	electron, either itinerant or bound
F	Faraday's constant ($C\,mol^{-1}$)
$h^{\cdot}$	electron hole
G	charge generation rate ($C\,cm^{-2}\,s^{-1}$)
i_0	exchange current density of ORR ($A\,cm^{-2}$)
i_{ORR}	local ORR current density ($A\,cm^{-2}$)
$i_{ORR}^{(e)}$	local ORR current density arising from participation of electrons ($A\,cm^{-2}$)
$i_{ORR}^{(h)}$	local ORR current density arising from participation of electron holes ($A\,cm^{-2}$)
i_{hom}	total cell current density expected in the case of a well current-collected test cell with the potential $\Delta\tilde{\mu}_e^*$ (CC) distributed homogeneously over the film ($A\,cm^{-2}$)
i_{sim}	simulated apparent total cell current density ($A\,cm^{-2}$)
$\hat{i}_e$	local current density in film cross-section due to electrons ($A\,cm^{-2}$)
$\hat{i}_h$	local current density in film cross-section due to electron holes ($A\,cm^{-2}$)
$\hat{i}_m$	total local current density in film cross-section ($A\,cm^{-2}$)
$\hat{i}_v$	local current density in film cross-section due to oxygen vacancies ($A\,cm^{-2}$)
$\hat{i}_{plane}$	total local current density in the 2D film representation ($A\,cm^{-1}$)
n	number of electrons transferred in the electrochemical reaction
O_O^x	occupied oxygen lattice site
R	universal gas constant ($J\,mol^{-1}\,K^{-1}$)
R_p	polarization resistance ($\Omega\,cm^2$)
R_p^{global}	global apparent polarization resistance ($\Omega\,cm^2$)
R_p^{local}	local polarization resistance ($\Omega\,cm^2$)
R_{tot}	total area-specific test cell resistance, $R_p + R_\Omega$, ($\Omega\,cm^2$)
R_{tot}^{global}	total global area-specific test cell resistance ($\Omega\,cm^2$)
R_{tot}^{ideal}	total ideal global area-specific test cell resistance, $R_p^{local} + R_\Omega^{ideal}$, ($\Omega\,cm^2$)
R_Ω	area-specific Ohmic resistance ($\Omega\,cm^2$)
R_Ω^{global}	global apparent area-specific Ohmic resistance ($\Omega\,cm^2$)
R_Ω^{ideal}	ideal open-circuit, area-specific Ohmic resistance, arising from resistance to ionic current in electrolyte, equal to t_e/σ_i ($\Omega\,cm^2$)
r_{ORR}	rate of the oxygen reduction reaction ($mol\,cm^{-2}\,s^{-1}$)
P_{O_2}	oxygen partial pressure (atm)
s	spacing between CC features (μm)
s_c	spacing between CC features leading to no more than a 0.5% increase of R_{tot} over R_{tot}^{ideal}(μm)
T	temperature (K)
t	time (s)
t_e	electrolyte thickness (μm)
t_m	MIEC film thickness (nm)
V_{cell}	cell voltage (V)
$V_O^{\cdot\cdot}$	oxygen lattice site vacancy
z_e	formal charge of electron, −1
z_h	formal charge of electron hole, +1
z_j	formal charge of charged species j
z_h	formal charge of oxygen vacancy, +2
$\overleftarrow{\alpha}$	anodic transfer coefficient
$\overrightarrow{\alpha}$	cathodic transfer coefficient
η	nominal global cathodic overpotential (V)
η_{local}	local cathodic overpotential, $\Delta\tilde{\mu}_e^* - \Delta\Phi_e$ (V)
ρ_{plane}	2D free charge density in the MIEC film ($C\,cm^{-2}$)
σ_e	electron conductivity of MIEC ($S\,cm^{-1}$)
σ_i	electrical conductivity of electrolyte ($S\,cm^{-1}$)
σ_h	electron hole conductivity of MIEC ($S\,cm^{-1}$)
σ_m	electrical conductivity of MIEC ($S\,cm^{-1}$)
σ_v	oxygen vacancy conductivity of MIEC ($S\,cm^{-1}$)
$\tilde{\mu}_e$	electron electrochemical potential in MIEC ($J\,mol^{-1}$)
$\tilde{\mu}_e^*$	scaled electron electrochemical potential in MIEC (V)
$\Delta\tilde{\mu}_e$	change of electron electrochemical potential from its equilibrium value in the MIEC ($J\,mol^{-1}$)
$\Delta\tilde{\mu}_e$ (CC)	$\Delta\tilde{\mu}_e$ at the CC ($J\,mol^{-1}$)
$\Delta\tilde{\mu}_e^*$	change of scaled electron electrochemical potential from its equilibrium value in the MIEC (V)
$\Delta\tilde{\mu}_e^*$(CC)	$\Delta\tilde{\mu}_e^*$ at the CC (V)
$\Delta\tilde{\mu}_e^*$ (far)	$\Delta\tilde{\mu}_e^*$ at the farthest point in the film from any CC (V)
$\tilde{\mu}_h$	electron hole electrochemical potential in the MIEC ($J\,mol^{-1}$)
$\tilde{\mu}_h^*$	scaled electron hole electrochemical potential in MIEC (V)
$\Delta\tilde{\mu}_h$	change of electron hole electrochemical potential from its equilibrium value in the MIEC (V)
$\Delta\tilde{\mu}_h^*$	change of scaled electron hole electrochemical potential from its equilibrium value in the MIEC (V)
$\tilde{\mu}_j$	electrochemical potential of charged species j in the MIEC ($J\,mol^{-1}$)
$\tilde{\mu}_j^*$	scaled electrochemical potential of charged species j in the MIEC equal to $\tilde{\mu}_j/(z_jF)$ (V)
$\tilde{\mu}_v$	oxygen vacancy electrochemical potential in the MIEC ($J\,mol^{-1}$)
$\tilde{\mu}_v^*$	scaled oxygen vacancy electrochemical potential in the MIEC (V)
$\Delta\tilde{\mu}_v^*$	change of scaled oxygen vacancy electrochemical potential from its equilibrium value in the MIEC (V)
ν	stoichiometry number of the reaction
$\Delta\Phi_e$	change of electrostatic potential of the electrolyte from its equilibrium value (V)
ω	angular frequency of signal (s^{-1})
∇	gradient operator

rate of electrochemical reaction, adding another layer of complication. These test cells are also required to function at a variety of temperatures, oxygen partial pressures, and polarizations which may change the governing properties – such as magnitude and type of conductivity – nonlinearly by orders of magnitude without any change to the manner of current collection. Therefore, some general guidance is still needed to elucidate how potential is distributed within mixed-conducting films of widely varying properties, how it affects cell kinetics, and how test cells may be designed to avoid interference from it. To the knowledge of the authors, these challenges have not been investigated in a systematic and general manner and thus the focus of this paper is of significant practical importance.

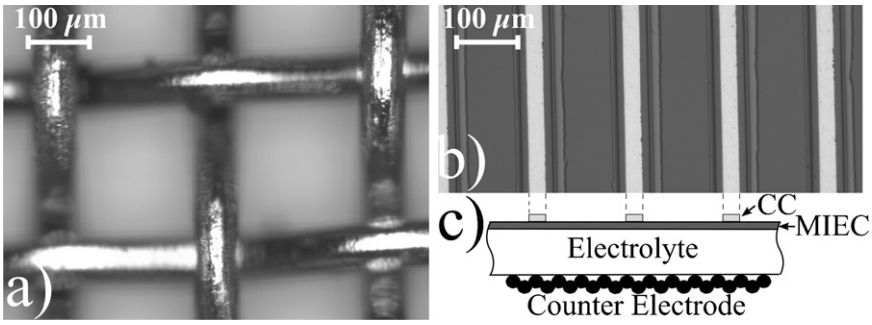

Fig. 1. (a) Optical micrograph of a typical woven CC mesh. (b) Optical micrograph (top view) and (c) schematic diagram (cross-sectional view) of a continuous LSM film test cell with patterned, parallel platinum CCs deposited on top. The LSM appears dark while the CCs appear silver. The clear covering on top of the CCs in (b) is a thin layer of undoped zirconia intended to block the platinum-LSM TPB and is not considered in the model.

The intention of this paper is to clarify the key issues and to provide a general and empirical theoretical modeling study of sheet resistance in thin-film test cells for test cell design. The approach is intended to be empirical rather than delving into the specifics of defect chemistry, reaction mechanisms, and other elemental characteristics in order to keep the analysis as generally applicable to a variety of candidate SOFC cathode materials as possible. To accomplish this task, the effect of various CC configurations on performance is elucidated and estimations of the geometry required to avoid a critical amount of sheet resistance under various cell configurations is given by mapping in parameter space.

2. Theory

2.1. Geometry

There are several ways to provide current collection to a test cell. Among them are removable methods, such as point contact by a microprobe [12,16,19,23,25] and the application of a platinum or gold mesh [1,3,8,10,13,14,17,18,22], which rely upon mechanical force to make a good contact. There are also non-removable methods, such as the deposition of a porous layer by printing, painting, or sputtering [15,26] and also the deposition of patterned CCs via photolithography and physical vapor deposition [20,21].

Point contact by a microprobe is very useful for conducting local microimpedance measurements, but the sheet resistance may be severe due to the current constriction around the probe [37] and therefore it is best used to investigate small MIEC islands. Deposition of a porous layer provides good current collection, but can interfere with gas diffusion and the introduction of large MIEC-CC triple phase boundary (TPB) length can add extraneous electrochemical processes to the cell.

Mesh and patterned CCs allow for freer MIEC surface area and fewer MIEC-CC TPBs, but may or may not inhibit sheet resistance depending on their spacing, the film thickness, and the MIEC's intrinsic properties. The free surface area, i.e. that not covered by CC, may be used for other forms of in situ characterization, such as Raman spectroscopy and X-ray analysis. This paper addresses mesh and patterned configurations with the goal of maximizing free surface area for in situ techniques while minimizing the effect of sheet resistance upon global EIS response.

Fig. 1 provides top-view optical micrographs of a mesh CC (a) and patterned CC lines (b, with side-view schematic c). Note that due to its woven nature, the mesh is likely to contact an MIEC only at certain, regularly spaced discrete areas where one wire crosses another as opposed to a continuously contacting grid. In contrast, the patterned CC lines in Fig. 1b provide intimate contact with the MIEC over their entire length. For the purpose of modeling, the discrete contacts are approximated here as circles. In Fig. 1a, the spacing between discrete contacts is approximately 270 μm.

A portion of a representative test cell is shown schematically in Fig. 2. The MIEC thin-film is deposited with thickness t_m onto a dense electrolyte (with thickness t_e) and the CC is deposited onto the top of the MIEC film. A porous catalyst layer on the bottom of the electrolyte serves as the counter electrode and is exposed to the same gaseous atmosphere as the working electrode. Three distinct CC configurations will be addressed. The "grid" configuration is depicted in Fig. 2a. The CCs are arrayed in two sets of mutually perpendicular lines, providing a network of continuous contacts. The distance between parallel lines is given by *s*, the CC spacing. The second configuration, "parallel," can be depicted if one set of intersecting CCs is removed from Fig. 2a, leaving only CC lines aligned in one direction. These two configurations can be achieved either by deposition via photolithography or from a removable, nonwoven CC mesh appropriately designed for continuous contacts and carefully applied to the surface. The third configuration, "discrete," is achieved if all of the CC lines from Fig. 2a are removed and replaced by small, circular contacts where the points of intersection had previously been. This case is an approximation of the contact pattern expected from a woven CC mesh (see Fig. 1a), where the mesh only makes contact in certain places. The current collection provided by a mesh, in reality, is probably actually somewhat intermediate

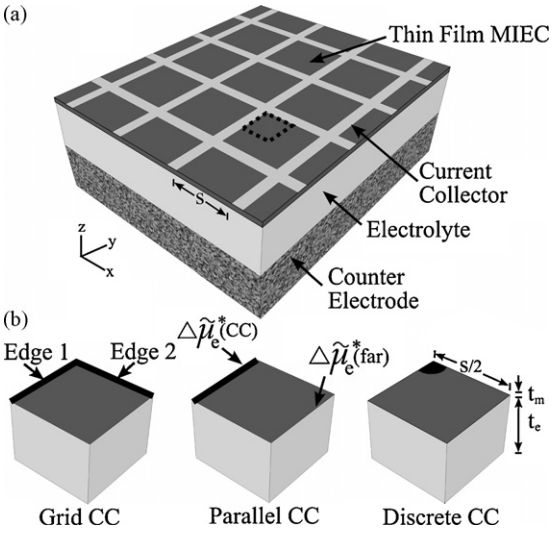

Fig. 2. (a) Schematic illustration of thin-film test cell geometry, with the thin-film MIEC deposited onto a dense electrolyte and CCs deposited in the "grid" configuration. The "parallel" CC configuration is achieved if one set of intersecting CCs is removed, leaving only parallel CCs. The "discrete" CC configuration is achieved if all of the CC lines are removed and replaced by small, circular contacts where the points of intersection had previously been. The distance between CCs is *s*. (b) Domains for FEM simulation, reduced from (a) by symmetry along the dashed line.

between the "discrete" and "grid" configurations depending on the pressure applied, wire diameter, etc.

The actual simulation domain (Fig. 2b) is a simplification from the overall geometry and is formed from the symmetry of the CCs, depicted by the dashed outline in Fig. 2a. For the grid configuration, the CC contact is along Edges 1 and 2. For the parallel configuration, it is along Edge 1. The discrete configuration's CC contact is within and on the boundary of the quarter-circle region only. The quantities $\Delta\tilde{\mu}_e^*(CC)$ and $\Delta\tilde{\mu}_e^*$ (far) represent the change to scaled electron electrochemical potential at the CC and far from the CC, respectively, and will be elaborated upon later.

2.2. Nature of MIECs

Candidate mixed-conducting SOFC cathode materials are generally in the perovskite family and show conductivity toward oxygen and electronic species. Oxygen conductivity is common to all of these materials, the transference number being different in each material, and takes the form of oxygen vacancies moving through the oxygen sublattice causing a net flow of O^{2-} in the direction opposite to the net vacancy flux.

Electronic conductivity is generally much larger than the ionic conductivity, but its origin is not the same in all of the materials. The electronic conductivity of $La_{1-x}Sr_xCoO_{3-\delta}$ (LSC), for example, is metallic in behavior and caused by itinerant electrons in a partially filled broad band [38]. Semiconductor-like behavior prevails in some compositions of LSM [39] and $La_{1-x}Sr_xFeO_{3\pm\delta}$ (LSF) [40,41], caused by the hopping of small polarons on the B-site. They are primarily p-type, with the positively charged defects ($B_B^{\cdot}$ in Kröger–Vink notation) as the majority carrier but with negatively charged defects (B_B') contributing as well.

The different origins of electronic conduction cause small but important differences in the mechanism of the oxygen reduction reaction (ORR). For instance, the overall ORR at the LSC surface may be written as

$$\frac{1}{2}O_2 + V_O^{\cdot\cdot} + 2e^- = O_O^x \tag{1}$$

where $V_O^{\cdot\cdot}$ is an oxygen vacancy and O_O^x is an occupied oxygen site (in Kröger–Vink notation), and e^- is an electron. The overall ORR at the surface of a hopping-type conductor may be written as

$$\frac{1}{2}O_2 + V_O^{\cdot\cdot} + qB_B^x + (2-q)B_B' = O_O^x + qB_B^{\cdot} + (2-q)B_B^x \tag{2}$$

where $q = 0, 1,$ or 2 depending on which electronic defects are involved. Generally, each different value of q causes distinct kinetics under a given set of experimental conditions and should be treated independently in an elemental model [42]. However, a treatment that is sufficiently general to seamlessly model the potential distribution within and the kinetics on the surface of these films, despite their differences in conduction and oxygen reduction, is desired and may be achieved through empirical means.

2.3. Potential distribution

In order to avoid specifics of defect chemistry and convolution of chemical and electrical effects (which in general will be different for every composition of MIEC), the change to the electrode potential is best related to the electrochemical potential of electrons in the working electrode, $\tilde{\mu}_e$, without further delineation. The change to $\tilde{\mu}_e$ from its equilibrium value is given by $\Delta\tilde{\mu}_e$. The cell voltage is given by $V_{cell} = \left|\Delta\tilde{\mu}_e(CC)/(z_eF)\right|$, where $\Delta\tilde{\mu}_e$ (CC) is $\Delta\tilde{\mu}_e$ at the CC upon application of the voltage, $z_e = -1$ is the formal charge of an electron, F is Faraday's constant, and $\Delta\tilde{\mu}_e > 0$ under cathodic polarization. A scaled electrochemical potential of a charged species j is given by $\tilde{\mu}_j^* = \tilde{\mu}_j/(z_jF)$, where z_j is the formal charge [43]. Then $V_{cell} = |\Delta\tilde{\mu}_e^*(CC)|$.

2.3.1. Metallic conduction in MIEC

In a metallic-conducting MIEC, the mobile charge carriers are electrons and oxygen vacancies. Thus, the total electrical current within the film, $\hat{i}_m$, is given by

$$\hat{i}_m = \hat{i}_e + \hat{i}_v \tag{3}$$

The currents arising from electrons and vacancies are expressed as $\hat{i}_e = -\sigma_e\nabla\tilde{\mu}_e^*$ and $\hat{i}_v = -\sigma_v\nabla\tilde{\mu}_v^*$, respectively, where σ_e and σ_v are the electron and vacancy conductivities. Since equilibrium electrochemical potentials are spatially uniform, the currents can be expressed in terms of departures from equilibrium values: $\hat{i}_e = -\sigma_e\nabla(\Delta\tilde{\mu}_e^*)$ and $\hat{i}_v = -\sigma_v\nabla(\Delta\tilde{\mu}_v^*)$. Considering that $\sigma_e \gg \sigma_v$ [44,45] and that $\|\nabla(\Delta\tilde{\mu}_e^*)\| \gg \|\nabla(\Delta\tilde{\mu}_v^*)\|$ (which can be shown taking the gradient of the electrochemical potentials of electrons and vacancies when expressed in the appropriate formalism [38]), then $\|\hat{i}_e\| \gg \|\hat{i}_v\|$ and thus

$$\hat{i}_m \approx \hat{i}_e = -\sigma_m\nabla(\Delta\tilde{\mu}_e^*) \tag{4}$$

where $\sigma_m \approx \sigma_e$ is the electrical conductivity of the MIEC material, available from a standard four-probe measurement.

Let $\hat{i}_{plane}$ be given by $\hat{i}_{plane} = \int_0^{t_m}\hat{i}_m\,dz$ where z is in the thickness direction of the film. Since the film is thin, $\nabla\tilde{\mu}_e^*$ can be assumed to be entirely contained in the x–y plane and zero in the z-direction, making $\hat{i}_m$ constant in the z-direction as well. Therefore

$$\hat{i}_{plane} = \hat{i}_m t_m = -\sigma_m t_m\nabla(\Delta\tilde{\mu}_e^*) \tag{5}$$

and the conduction equation is transformed from 3D to 2D (in the x–y plane).

The conservation of charge requires that

$$\frac{\partial\rho_{plane}}{\partial t} = -\nabla\cdot\hat{i}_{plane} + G \tag{6}$$

where ρ_{plane} is the 2D free charge density in the MIEC film ($C\,cm^{-2}$), t is time (s), $\hat{i}_{plane}$ is the current density in the film ($A\,cm^{-1}$), and G is the charge generation rate ($C\,cm^{-2}\,s^{-1}$).

Since the film is thin and vacancy transport in the x–y plane is relatively small, all vacancies entering the MIEC from the electrolyte are approximately transported in the z-direction only and eventually consumed by the ORR at the MIEC-air surface. At steady state, the rate of vacancy injection is equal to the rate of vacancy consumption and thus vacancies contribute nothing to G. In contrast, electrons are constantly consumed at the MIEC-air surface by the ORR and there is a net consumption of negative charge, or effective positive charge generation, that contributes to G on the local level. This contribution to G is effectively a current, proportional to the product of n, the number of electrons in Eq. (1) ($n = 2$) and the rate of the reaction, r_{ORR}. Denote this quantity i_{ORR} where

$$i_{ORR} = nFr_{ORR} \tag{7}$$

and has units of C cm^{-2} s^{-1} or, equivalently, A cm^{-2}. Finally, at steady state, $\partial\rho_{plane}/\partial t = 0$. This leaves

$$0 = \nabla\cdot(\sigma_m t_m\nabla(\Delta\tilde{\mu}_e^*)) + i_{ORR} \tag{8}$$

as the equation that must be solved in the 2D representation of the MIEC film for the variable $\Delta\tilde{\mu}_e^*(x)$. Fig. 3 shows a schematic diagram of the flow of charge, including electrons, e', and oxygen vacancies, $V_O^{\cdot\cdot}$, within the film to an active site on the surface.

On the boundary, the potential is fixed at the contact with the CC. In the grid configuration, the potential is fixed along both Edge 1 and 2 (Fig. 2b), with $\Delta\tilde{\mu}_e^*(CC) = -V_{cell}$. In the parallel configuration, the potential is fixed only at Edge 1. In the discrete configuration, the potential is fixed within and along the boundary of the

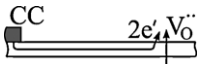

Fig. 3. Schematic diagram of the flow of charge in the oxygen reduction reaction. Oxygen vacancies travel in the through-thickness direction, from the electrolyte to the surface. Electrons travel in the in-plane direction from the CC and are consumed at the reaction site.

quarter-circle region only. The free edges in each configuration are symmetric (Neumann) boundaries. The value of $\Delta\tilde{\mu}_e^*$ at the point in the film farthest from the CC is a dependent variable and is given special notation $\Delta\tilde{\mu}_e^*(\text{far})$.

2.3.2. Semiconduction in MIEC

MIEC materials with semiconductor-like behavior present a slightly more complicated situation than those with metallic conduction. In these materials, electrons, electron holes, and oxygen vacancies comprise the set of mobile charge carriers. Thus, the total current is given by

$$\hat{i}_m = \hat{i}_e + \hat{i}_h + \hat{i}_v \tag{9}$$

where $\hat{i}_e$ is the current from electrons (i.e. negatively charged small polarons, B_B'), and $\hat{i}_h$ is the current from electron holes (i.e. positively charged small polarons, $B_B^{\cdot}$). The following analysis is valid for semiconduction arising via broad bands as well.

Similarly to the case of metallic conduction, $\|\hat{i}_v\| \ll \|\hat{i}_m\|$ (shown by considering the relative magnitude of σ_v vs. σ_m [46] as well as the configurational contribution to diffusion). Thus,

$$\hat{i}_m \approx \hat{i}_e + \hat{i}_h = -\sigma_e\nabla(\Delta\tilde{\mu}_e^*) - \sigma_h\nabla(\Delta\tilde{\mu}_h^*) \tag{10}$$

where σ_h is the electron hole conductivity. The electron and hole electrochemical potentials are connected to one another through local equilibrium. The reaction can be written as

$$2B_B^x \rightleftarrows B_B^{\cdot} + B_B' \tag{11}$$

Local equilibrium requires

$$\Delta\tilde{\mu}_h = -\Delta\tilde{\mu}_e \tag{12}$$

Scaling the electrochemical potentials, $\Delta\tilde{\mu}_h^* = \Delta\tilde{\mu}_e^*$. Finally, $\nabla(\Delta\tilde{\mu}_h^*) = \nabla(\Delta\tilde{\mu}_e^*)$. Thus, the total current may be expressed as

$$\hat{i}_m \approx -(\sigma_h + \sigma_e)\nabla(\Delta\tilde{\mu}_e^*) \approx -\sigma_m\nabla(\Delta\tilde{\mu}_e^*) \tag{13}$$

with Eq. (5) applicable, making $\hat{i}_{plane}$ equivalent to the metallic conduction case.

On the surface, assume that both electrons and holes may participate in the ORR to different degrees, with either electrons being consumed or holes being injected. Both processes have the effect of a local increase in positive charge and therefore i_{ORR} in this case is given by

$$i_{ORR} = i_{ORR}^{(h)} + i_{ORR}^{(e)} \tag{14}$$

Eq. (6) is used again with $G = i_{ORR}$ defined by Eq. (14). The final result is exactly equivalent to Eq. (8) with $\Delta\tilde{\mu}_e^*(x)$ as the desired quantity.

2.3.3. Mixed metallic and semiconducting behavior

Some candidate cathode MIECs, e.g. $La_{1-x}Sr_xCo_{1-y}Fe_yO_{3-\delta}$ (LSCF), show a hybrid conduction mechanism of both metallic and semiconducting character [47]. By following analogous logic to that laid out in the previous two sections and recognizing the minor contribution of oxygen vacancies to total conductivity [46,48], it can be shown that Eq. (8) is the governing equation and that $\Delta\tilde{\mu}_e^*$ specifies the electrical state of the MIEC film.

2.3.4. Ionic conduction in electrolyte

In the electrolyte, Eq. (15) suffices in the 3D domain assuming no changes in bulk chemical composition

$$0 = \nabla\cdot(\sigma_i\nabla(\Delta\Phi_e)) \tag{15}$$

where σ_i is the electrical conductivity of the electrolyte, in the case of SOFC test cells due primarily to oxygen vacancies, and $\Delta\Phi_e$ is the departure of electrostatic potential from its equilibrium value. The boundary condition along the electrolyte–MIEC interface is given by the current out: $i_{ORR} = z_v F r_{ORR}$, where z_v is the formal charge of an oxygen vacancy. The bottom electrolyte boundary is Dirichlet, with $\Delta\Phi_e = 0$. The side faces are symmetric boundaries.

2.4. Interfacial polarization due to oxygen reduction at open-circuit voltage

The strategy for estimating i_{ORR} at open-circuit voltage (OCV) is linked to the simple, empirical, and linear measurement of the polarization resistance, R_p, obtained by EIS. Fig. 4a is a schematic of a complex impedance plot that could belong to a test cell. R_Ω is the Ohmic resistance, generally assumed to result primarily from the resistance to ionic conduction in the electrolyte. R_p is generally assumed to correspond to the overall chemical/electrochemical process of oxygen reduction. At steady state, these values add to total resistance, R_{tot}.

In general, the complex impedance response of thin films, even on a local level, is not trivial. Some variation of the equivalent circuit shown in Fig. 4b has been proposed in a number of studies to account for the kinetics of several different candidate materials, including LSC, LSCF, and LSM [7,12,13,16–18,23,43]. Such an equivalent circuit, distributed over a 2D film, is useful for envisioning the local response of an electrode on an empirical basis [49,50], as demonstrated in Fig. 4c. The local responses may be summed to obtain the global response at various frequencies.

Under steady state conditions (angular frequency $\omega = 0$), even complicated local equivalent circuits may simplified by a single effective resistor (Fig. 4d). As long as a simulation is limited to the steady state condition, this concept can be used to explore sheet resistance without having to speculate too much about the nature of the equivalent circuit. That is, a simple resistor distributed over the 2D film can describe all ORR processes at steady state. The local effective resistance, R_p^{local}, may or may not be close to the global polarization resistance, R_p^{global}, of the cell depending on the impact of the sheet resistance.

At small overpotential (tens of mV), it is assumed that the response is linear and that the macroscopic ORR kinetics of the test cell may be approximated by a linear relationship between the

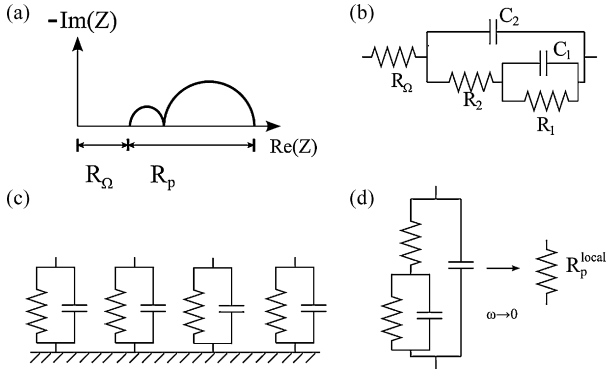

Fig. 4. (a) Schematic of a possible complex impedance plot of a test cell. (b) Typical equivalent circuit assigned to MIEC film reaction kinetics. (c) Local RC elements distributed on a surface. (d) Reduction of 1D equivalent circuit to a single resistor when $\omega \to 0$.

local cathodic overpotential, η_{local}, and current by way of R_p^{local}

$$i_{ORR} = \frac{|\eta_{local}|}{R_p^{local}} \quad (16)$$

The local cathodic overpotential η_{local} is defined as

$$\eta_{local} = \Delta\tilde{\mu}_e^* - \Delta\Phi_e \quad (17)$$

and couples together the electrolyte and MIEC.

With the use of thin films for fundamental SOFC investigations, it is often assumed that the global Ohmic resistance, R_Ω^{global}, is the result of resistance in the electrolyte. The impedance loop is assumed to arise from local electrochemical processes. Unfortunately, sheet resistance can impact both of these quantities, causing R_Ω^{global} to increase and additional features to enter the impedance loop through time constant dispersion. This time constant dispersion has been observed as an effect of potential distribution for the rotating disk electrode in aqueous electrochemistry [49,50]. Dispersion has also been cited in solid-state systems due to current constriction [37]. In general, additional impedance features tend to increase the global resistance and without proper care they can be interpreted as part of the fundamental kinetics of a candidate material.

For a brief look at the effect of sheet resistance in our thin-film working electrodes at high frequency, we deviate momentarily from our steady state treatment and for the purpose of example assume a local equivalent circuit with resistor and capacitor in parallel (Fig. 4c). We then simulate a global EIS response over a broad frequency range for the discrete CC configuration (Fig. 5), allowing the local capacitors to contribute to G in Eq. (6), enforcing $\partial\rho_{plane}/\partial t = 0$, and solving for complex variables. Further details of numerical implementation are given in Section 2.6.

The quantity $(t_m\sigma_m)$ is used as a figure of merit to assess the conductance of the film and demonstrate the effect of lower conductance on the EIS spectrum. A smaller value indicates more sheet resistance interference. The largest $(t_m\sigma_m)$ in Fig. 5 has a global EIS spectrum that is semicircular, nearly perfectly reflecting the ideal local behavior and with a slight Ohmic resistance caused by the thin electrolyte. As $(t_m\sigma_m)$ decreases, sheet resistance causes a time constant dispersion resulting in an increased Ohmic resistance as well as a second semicircle appearing in the loop at high frequency. The new, extraneous impedance feature can become a large component of the loop, e.g. $(t_m\sigma_m) = 1 \times 10^{-4}\ \Omega^{-1}$, the lowest value of $(t_m\sigma_m)$ shown in the plot. The extraneous loop can dominate the spectrum at even lower film conductance.

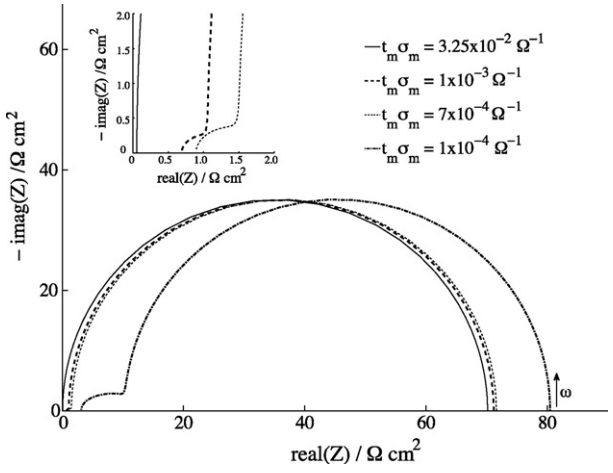

Fig. 5. Simulated global EIS spectra at different values of $(t_m\sigma_m)$ for a thin-film with discrete current collector configuration. $s = 500\ \mu m$, $t_e = 1\ \mu m$, $R_p^{local} = 70\ \Omega\ cm^2$, distributed local capacitance $= 0.02\ F\ cm^{-2}$, and ω range 10^{-5} to 1.6×10^4 Hz. The inset plot is a magnification of the high-frequency region.

The alteration of the EIS spectrum is associated with a simultaneous increase of the total steady state resistance (R_{tot}, the low-frequency real(Z) intercept). There is no second feature discernible for the largest $(t_m\sigma_m)$, and so R_{tot} is shifted merely 0.05% from R_{tot}^{ideal}. We define R_{tot}^{ideal} as

$$R_{tot}^{ideal} = R_p^{local} + R_\Omega^{ideal} \quad (18)$$

where $R_\Omega^{ideal} = t_e/\sigma_i$. The spectra associated with $(t_m\sigma_m) = 1 \times 10^{-3}\ \Omega^{-1}$ and $7 \times 10^{-4}\ \Omega^{-1}$ are shifted from R_{tot}^{ideal} by 1.5 % and 2.1%, respectively. The shift caused by $(t_m\sigma_m) = 1 \times 10^{-4}\ \Omega^{-1}$ is 14.8%. Even lower conductances lead to larger shifts from R_{tot}^{ideal} due to the dominance of the extraneous high-frequency feature.

The additional features contain no intrinsic significance relevant to the ORR, yet they may easily be confused with features arising from adsorption of oxygen at the film surface or with other chemical processes. The goal of this contribution is to guide cell design in such a way that electrochemical uniformity may be maintained in the film without sheet resistance interference under high or low frequency conditions so that the global EIS spectrum may be used to accurately interpret local electrochemical phenomena. We use the proximity of the actual simulated total resistance, R_{tot}, to R_{tot}^{ideal} as a measure of the impact of sheet resistance. We define R_{tot} as

$$R_{tot} = \frac{V_{cell}}{i_{sim}} \quad (19)$$

where i_{sim} is the calculated total apparent current density of the cell, that is

$$i_{sim} = \frac{\int_{MIEC}(i_{ORR})\,dA}{A_{active}} \quad (20)$$

The numerator is the integral of the local ORR current density taken over the active MIEC surface (i.e. the total ORR current) and the denominator is the area of the active MIEC surface.

The case generally assumed by experimentalists is sought, i.e. $R_p^{global} \approx R_p^{local}$ and $R_\Omega^{global} \approx R_\Omega^{ideal}$. A deleterious role of sheet resistance would tend to make R_{tot} larger than R_{tot}^{ideal} as a consequence of additional, interfering high-frequency impedance features that force these approximate equalities to be untrue. In the previous example, we assumed a specific equivalent circuit. The exact nature of appropriate circuits will be different from material to material and need not further concern us. Specifics aside, the observation that undesirable high-frequency features can arise and are associated with an increase in R_{tot} can be generalized when we seek to limit the steady state change to R_{tot}.

Having some estimate of R_p^{local} is important, as its value determines i_{ORR}, which is directly proportional to sheet resistance. Obviously, since the purpose of this contribution is to aid in accurately measuring R_p^{local}, a precise value is not expected. Fortunately, only an estimate from a rough EIS measurement, possibly found in the literature on the specific or a related system, may suffice for general guidance on CC spacing. Getting a good estimate for this value experimentally may or may not be trivial, depending on the material. For instance, R_p of the LSC–LSCF family is relatively insensitive to film thickness at intermediate to high temperatures (provided sheet resistance is mitigated) [5,8,13]. Hence, R_p measured from a relatively thick film can be used as an estimate in Eq. (16). On the other hand, R_p of LSM is very sensitive to thickness [3,4,16]. Simply increasing thickness to minimize sheet resistance will also result in an altered R_p and an adjustment, e.g. linear correlation with thickness [4], may be required to estimate R_p. Furthermore, R_p is also well-known as a function of temperature, T, and oxygen partial pressure, P_{O_2}. It is more conservative to underestimate R_p^{local} if the goal is to minimize sheet resistance.

2.5. Large-polarization approximation

Any model for large cathodic polarization requires more input than the small polarization case. Unfortunately, behavior under large cathodic polarization is very specific to individual materials. Experimental measurements can provide current–voltage data and a succession of impedance data at intermediate polarizations. These measurements should be conducted in a geometry where sheet resistance is as minimized as possible in order to translate them directly to the local environment. The impedance data can then be used to separate R_Ω from R_p and hence identify the nominal global cathodic overpotential, η, as a component of the cell voltage. A table of cell current density vs. η may then be constructed, from which $i_{ORR} = i(\eta_{local})$ may be interpolated for local use in the model. This approach is very specific to the material under investigation and likely cannot be generalized to others that differ in composition or electrochemical history, but is the best approach when such data is available.

Alternatively, in exchange for more assumptions, a kinetic model may be applied to determine $i_{ORR}(\eta_{local})$. We take this approach here in order to demonstrate the effect of large polarization. Because test cells often display some exponential character in the current–voltage relationship of dense films [3,4,7], the Butler–Volmer (BV) equation [51]

$$i_{ORR} = \left| i_0 \left(\exp\left(\overleftarrow{\alpha} \frac{F}{RT} \eta_{local} \right) - \exp\left(-\overrightarrow{\alpha} \frac{F}{RT} \eta_{local} \right) \right) \right| \tag{21}$$

will be applied locally here, though it typically is not used in conjunction with thin MIEC films. The variable i_0 is the exchange current density, R is the universal gas constant, T is the temperature, and $\overleftarrow{\alpha}$ and $\overrightarrow{\alpha}$ are the anodic and cathodic transfer coefficients, respectively. The transfer coefficients are related: $\overleftarrow{\alpha} + \overrightarrow{\alpha} = n/\nu$, where n is the number of electrons transferred in the overall reaction and ν is the stoichiometry number, that is the total number of times the rate-limiting step occurs in the overall reaction. Consider the reaction shown in Eq. (1). Lacking other information, let $n = 2$ and $\nu = 1$. Then, $\overleftarrow{\alpha} + \overrightarrow{\alpha} = 2$. For simplicity, let $\overleftarrow{\alpha} = \overrightarrow{\alpha} = 1$. The exchange current density can be estimated from R_p^{local}

$$i_0 = \frac{1}{R_p^{local}} \frac{\nu RT}{nF}. \tag{22}$$

The BV equation here serves as an empirical estimation of the large-polarization case and likely overestimates the local current density of many solid-state MIEC electrodes due the fact that specific kinetic limitations, such as mass transport, the intricacies of defect chemistry, and chemical processes at the MIEC surface, are not taken explicitly into consideration. Delving into these issues would require a more sophisticated 3D elemental model [28,29,52], which is useful for probing specific materials on a fundamental level and is the subject of continued development but is beyond the simple, empirical, and general scope of this paper. The purpose of using BV here is simply for some model to link η_{local} to i_{ORR} superlinearly. We recommend a more detailed model for use with a specific material if large cathodic polarization is of interest. However, this approach is certainly accurate in the case where charge-transfer kinetics apply explicitly, especially in other thin-film electrochemical systems.

For the purpose of this model, constant σ_m is assumed. In reality, when the oxygen stoichiometry of a typical MIEC material is altered, say by varying partial pressure of oxygen or temperature, the conductivity is known to change [53]. A similar change in conductivity is expected under cathodic polarization; however, very little is known about how it trends as a function of cathodic overpotential. Constant σ_m is therefore assumed in this model as the best available treatment and for generality.

2.6. Numerical implementation

The finite element method (FEM) with adaptive mesh refinement is employed for numerical simulations using the commercial software package Comsol Multiphysics version 3.5a. The simulations were performed on the domains shown schematically in Fig. 2b, which were modeled using the software's computer aided design (CAD) tools. The MIEC thin-film is simplified from a 3D volume with an extreme aspect ratio to a 2D surface, on which Eq. (8) is solved using Comsol's "weak form, boundary" application mode. Eq. (15) is solved in 3D in the electrolyte. The weak form boundary mode allows the top surface of the electrolyte block to serve as both the electrolyte boundary as well as the 2D MIEC film domain. The two domains are linked by the local current, a boundary expression. During solution, both the bulk and surface FEM problems are solved simultaneously. In cases with frequency dependence, the parametric solver may be used to simulate over all required frequencies. For further details, the software help file contains specifics of rendering model geometry, implementing constitutive equations and boundary conditions, meshing, and solving.

Values of CC spacing, s, or electrolyte thickness, t_e, that are far apart in magnitude cause the simulated geometry to be difficult to draw, mesh, and solve in the FEM software. In order to ease these computational limitations, σ_m and i_{ORR} in Eq. (8) and σ_i in Eq. (15) are scaled in the x, y, and z directions. The test cell is constructed once in the software's CAD application as a configuration that is convenient to mesh and solve. In order to change the geometry of the simulated physical test cell, the effective conductivity and effective local electrochemical current density is altered rather than the model domain shape to change the geometry of the test cell.

In the specific case of the test cell, let the physical CC separation in the x-direction be given by $s_x^{(physical)}$ and let the illustrated value in the CAD drawing be given by $s_x^{(model)}$. Similarly, the y-direction values are $s_y^{(physical)}$ and $s_y^{(model)}$, respectively. In the electrolyte, let the physical thickness be $t_e^{(physical)}$ while the illustrated thickness is $t_e^{(model)}$. Then, the scaling factors in the x-, y-, and z-directions are given by

$$f_x = \frac{s_x^{(physical)}}{s_x^{(model)}} \qquad f_y = \frac{s_y^{(physical)}}{s_y^{(model)}} \qquad f_z = \frac{t_e^{(physical)}}{t_e^{(model)}}. \tag{23}$$

The scaled, effective conductivities in the MIEC are

$$\sigma_{m,x}^{(eff)} = \sigma_m \left(\frac{f_y}{f_x} \right) \qquad \sigma_{m,y}^{(eff)} = \sigma_m \left(\frac{f_x}{f_y} \right) \tag{24}$$

and the scaled, effective conductivities in the electrolyte are

$$\sigma_{i,x}^{(eff)} = \sigma_i \left(\frac{f_y f_z}{f_x} \right) \qquad \sigma_{i,y}^{(eff)} = \sigma_i \left(\frac{f_x f_z}{f_y} \right)$$
$$\sigma_{i,z}^{(eff)} = \sigma_i \left(\frac{f_x f_y}{f_z} \right). \tag{25}$$

The local effective boundary current is

$$i_{ORR}^{(eff)} = (f_x f_y) i_{ORR} \tag{26}$$

due to the compression of the actual surface area in the CAD model by a factor of $f_x f_y$. This adjustment must be made in order to preserve the total current. The effective values are inserted into Eqs. (8) and (15). The tensor form of the FEM is then used to solve them. This approach makes it relatively easy to change s and t_e and in some cases is the only way to effectively simulate large aspect ratios by FEM. The scaling yields good agreement when tested against the full-scale simulation for different physical geometry test cases.

Table 1
Example film test cell parameters based on LSCF.

Parameter	Value	Units	Description
t_m	1	μm	MIEC film thickness
t_e	300–400	μm	Electrolyte film thickness
R_p	24.8	Ω cm^2	Open-circuit polarization resistance
R_Ω	9.3	Ω cm^2	Open-circuit Ohmic resistance
σ_m	325	S cm^{-1}	MIEC electrical conductivity [a]

[a] Conductivity value from the literature [55].

3. Results and discussion

In the following discussion, the model is used to first investigate the effect of various geometric and experimental parameters upon sheet resistance and cell performance and then it is used to provide generalized guidance on cell design.

3.1. Parameter investigation

For the parameter investigation, the data from an LSCF film deposited by sputtering onto a gadolinia-doped ceria (GDC) electrolyte substrate and using a mesh CC (Table 1) is used to illustrate specific trends. The value of σ_i was determined from R_Ω using the geometry of the electrolyte. In general, the input parameters vary as a function of the material as well as processing and experimental conditions, but the qualitative trends will be the same as those illustrated in this section. The reader is referred to the following section for guidance based upon specific configuration.

Potential distributions at steady state in each of the three CC configurations are given in Fig. 6, generated using the $t_m = 20$ nm and $s = 270$ μm, and a cell voltage of 10 mV (linear model). Each map was constructed by stitching together 16 simulation domains along the symmetric boundaries. In each CC configuration, the potential deviates from $\Delta\tilde{\mu}_e^*$ (CC), with more deviation as distance from the CC increases, attaining value $\Delta\tilde{\mu}_e^*$ (far) at the farthest point from the CC. The decreasing potential deviation in Fig. 6a–c shows that intra-film current collection is superior in the grid CC configuration and inferior in the 20-μm diameter discrete configuration when everything else is equal. The film with the discrete configuration sees a rapid change in potential away from the CC due to the effect of current constriction. The parallel configuration causes less current constriction than the discrete contacts and the average distance between a point on the surface and the CC is smaller. As a consequence, the potential deviates less from $\Delta\tilde{\mu}_e^*$ (CC) in the parallel configuration than in the discrete and hence sheet resistance is less severely manifested. The grid configuration experiences less sheet resistance than the previous two configurations for the same reason.

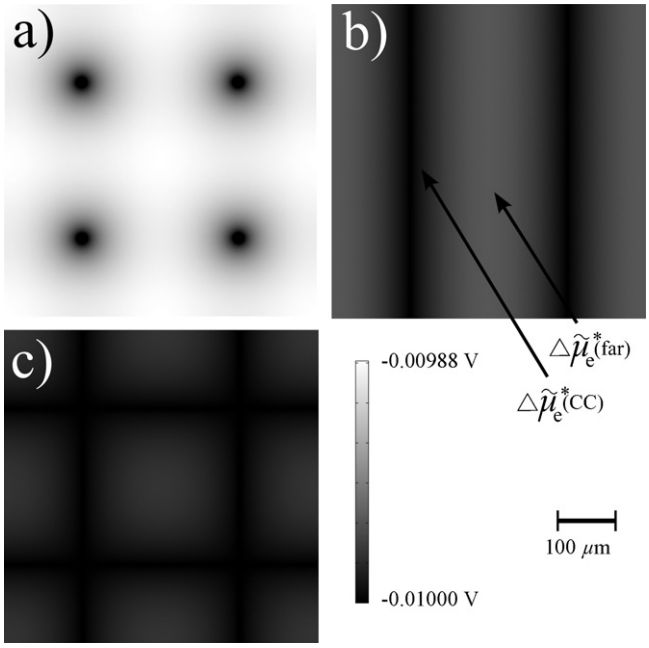

Fig. 6. Distribution of $\Delta\tilde{\mu}_e^*$ in the film for three CC configurations: (a) 20-μm diameter discrete contacts, (b) parallel, and (c) grid. R_p and σ_m from Table 1. Electrolyte is assumed very thin. $t_m = 20$ nm, $s = 270$ μm, $V_{cell} = 10$ mV.

One measure of the degree of sheet resistance is the steady state relative potential far from the CC, defined as

$$\text{Relative potential} \equiv \frac{\Delta\tilde{\mu}_e^*(\text{far})}{\Delta\tilde{\mu}_e^*(\text{CC})} \tag{27}$$

The relative potential is essentially the fraction of the applied potential retained by the MIEC far away from the CC. Another measure is the relative cell current

$$\text{Relative current} \equiv \frac{i_{sim}}{i_{hom}} \tag{28}$$

where i_{sim} is the simulated total apparent steady state cell current density from Eq. (20) and i_{hom} is the homogeneous cell current density expected in the case of a well current-collected test cell with the potential $\Delta\tilde{\mu}_e^*$ (CC) distributed homogeneously over the film (and hence no sheet resistance). That is, $i_{hom} = V_{cell}/(R_{tot}^{ideal})$. The relative current is the degree to which sheet resistance affects the global current response of the cell.

A similar global measure is the relative resistance

$$\text{Relative resistance} \equiv \frac{R_{tot}}{R_{tot}^{ideal}} \tag{29}$$

where R_{tot} is from Eq. (19) and R_{tot}^{ideal} is from Eq. (18).

The effect of cell geometry at small cell voltage (10 mV) is illustrated using these measures in Fig. 7. When the film is sufficiently thick (hundreds of nanometers to microns), the steady state potential does not deviate substantially from that applied at the CC (Fig. 7a). As the film becomes thinner, the potential deviates more severely from the applied value and the relative potential decreases. The consequence of this deviation is that the local overpotential far from the CC is reduced, resulting in a reduction in the local i_{ORR} and impacting the global relative current and relative resistance. The variation of cell current and resistance illustrates that sheet resistance has the capability to significantly alter the global response of a test cell.

Fig. 7b shows that both film thickness and CC spacing have a significant impact upon the apparent resistance of the cell. Close CC spacings alleviate the effect of small film thickness. Given CCs sufficiently close to one another, sheet resistance affects the relative resistance very little despite even small thickness and therefore sheet resistance can be neglected in subsequent data interpretation. Likewise, thicker films mitigate sheet resistance. Larger CC spacings and thinner films, though, exaggerate deactivation far from the CC. In general, the effect of sheet resistance becomes worse as the CC-spacing-to-film-thickness ratio increases. If the ratio is large enough, the resistance can be several times its ideal value.

Electrolyte thickness, t_e, also impacts sheet resistance in the cell (Fig. 7c). The small-t_e limit comes about when the electrolyte becomes so thin that its contribution to cell resistance is negligible. Therefore, the cell voltage is converted almost directly into cathodic overpotential, which drives large i_{ORR} across the cell. The large current density causes more severe sheet resistance in the film. Subsequent analysis in this contribution assumes that the electrolyte is vanishingly thin in order to deal with the worst case of sheet resistance.

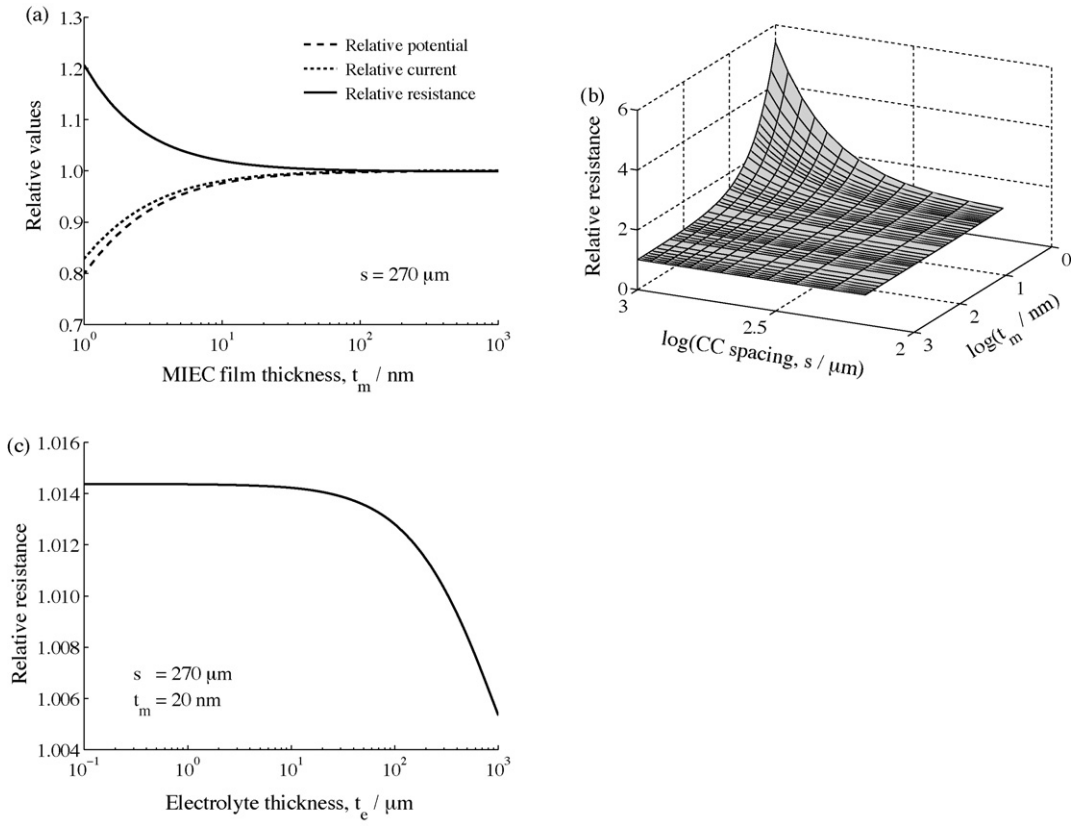

Fig. 7. (a) Relative values of potential, cell current, and resistance near OCV as a function of t_m for $s = 270\,\mu$ m under small cathodic polarization. (b) Relative resistance as a function of s and t_m. For (a) and (b), R_p^{local}, R_Ω, σ_m, σ_i, and t_e from Table 1. $V_{cell} = 10$ mV. (c) Effect of the electrolyte thickness on the relative resistance in the MIEC thin-film for different cell voltages. $t_m = 20$ nm and $s = 270\,\mu$m. R_p^{local}, σ_m, and σ_i from Table 1. 20-μm-diameter discrete CC configuration for all.

Under large cathodic bias (Fig. 8) the trends in relative potential, current, and resistance are similar to varying t_m (Fig. 7). However, a small change to local overpotential is magnified into a much larger change in the global quantities due to the exponential character of the assumed kinetics. Resistance away from OCV is defined as

$$R_{tot} = \frac{\partial V_{cell}}{\partial i_{sim}} \tag{30}$$

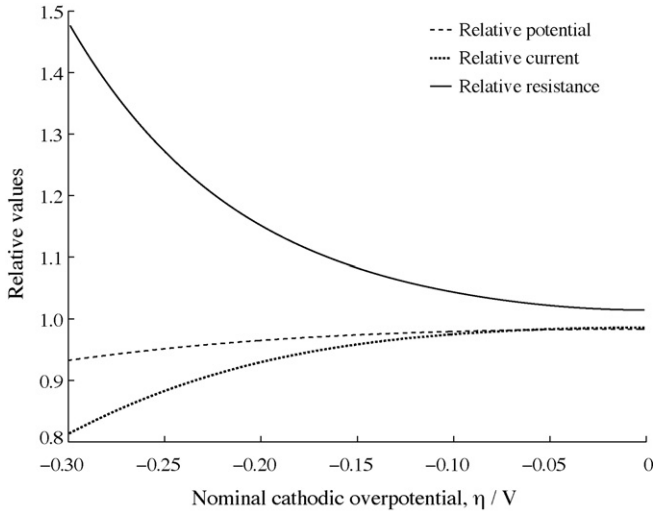

Fig. 8. Relative potential, relative cell current, and relative calculated total resistance as a function of nominal global cathodic overpotential (large-polarization kinetics) using the 20-μm diameter discrete CC configuration. The electrolyte is assumed vanishingly thin. $t_m = 20$ nm, $s = 270\,\mu$m. R_p^{local} and σ_m from Table 1.

The resistances used in computing the relative resistance in Fig. 8 are approximated using discrete data by computing a center difference

$$R_{tot}(V_j) = \frac{V_{cell,j+1} - V_{cell,j-1}}{i_{sim,j+1} - i_{sim,j-1}}. \tag{31}$$

around the data pair ($V_{cell,j}$, $i_{sim,j}$).

3.2. General cell design

The principal experimental factors affecting thin-film test cell response are

1. CC configuration (grid, parallel, discrete).
2. CC spacing, s.
3. MIEC film thickness, t_m.
4. Electric conductivity of the MIEC, σ_m.
5. Local polarization resistance, R_p^{local}.
6. Electrolyte thickness, t_e, and conductivity, σ_i.
7. Cell voltage, V/cathodic overpotential, η.

Many of these parameters can be manipulated in such a way that general information on sheet resistance can be extracted. We now develop maps computed from parameter encapsulation, inspired by those often employed for materials selection in mechanical design [54], that can be applied to arbitrary thin-film SOFC cathode MIEC candidates for the selection of CC spacing.

3.2.1. Small cathodic polarization

The following steps may be taken to simplify and generalize the small cathodic polarization case. At small polarization, both R_p^{local}

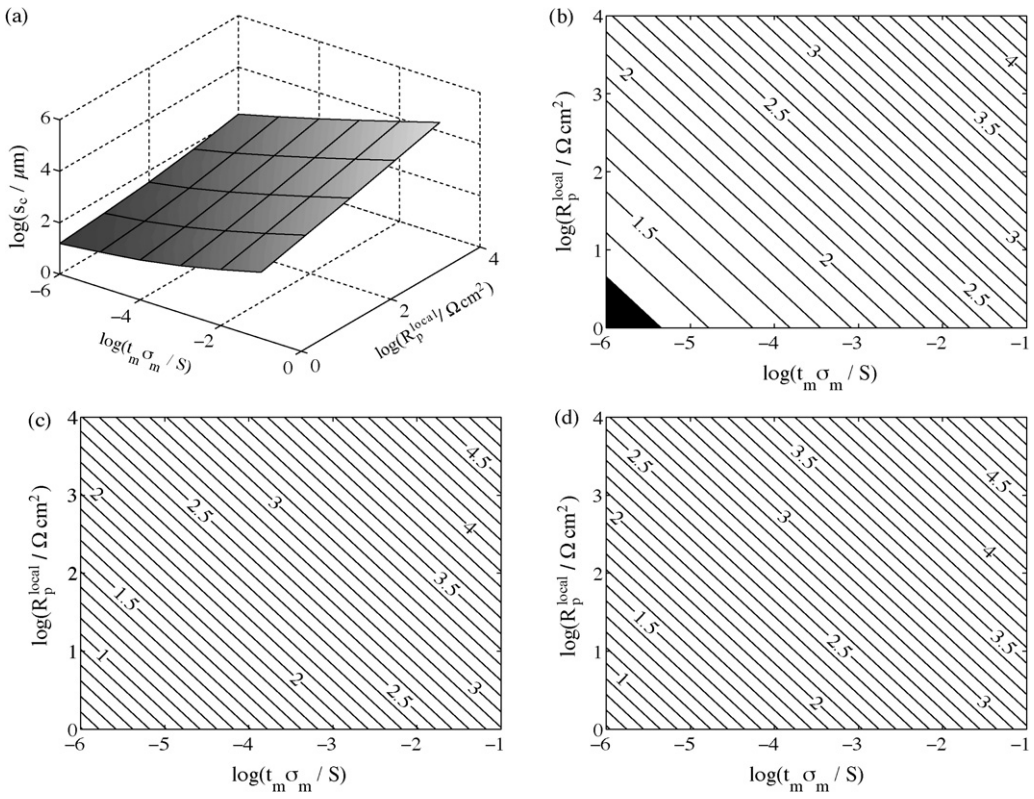

Fig. 9. (a) 3D surface of $\log(s_c)$ for the 20-μm diameter discrete CC configuration under small cathodic polarization. (b–d) Contour plots of $\log(s_c)$ for the (b) 20-μm diameter discrete, (c) parallel CC, and (d) grid CC configurations. The contours denote the level sets of $\log(s_c)$. The units of s_c are μm.

and σ_m are functions of temperature, oxygen partial pressure, and sometimes t_m. Because the structure of the model is such that R_p^{local} and σ_m are input directly from measurement or estimation, the other factors may be used to estimate R_p^{local} and σ_m for the desired experiment. Secondly, from Eq. (8), t_m and σ_m appear together. Therefore, they may be lumped into one parameter, $(t_m\sigma_m)$, as discussed previously. Next, as shown in Fig. 7c, if $t_e = 0$ and/or σ_i is very large, then sheet resistance in the MIEC film is maximized. Therefore, the electrolyte is assumed vanishingly thin in order to get a conservative estimate of the sheet resistance. Finally, the response is linear with η around OCV, so any choice of small $\Delta\tilde{\mu}_e^*(CC)$ should do; $\Delta\tilde{\mu}_e^*(CC) = -10$ mV is chosen.

Now, assume a specific CC configuration. If a particular relative resistance is desired and the variables R_p^{local} and $(t_m\sigma_m)$ are specified, then s must take on a unique value in order to satisfy the conditions imposed. Let this critical value of s be denoted s_c. Further analysis assumes that s_c is the value of s such that $R_{tot} = 1.005 \cdot R_{tot}^{ideal}$. We choose a 0.5% deviation from the ideal because it allows very few extraneous high-frequency features to be introduced but allows reasonable CC spacings to be retained. Similar plots can be generated with stricter or looser requirements.

Fig. 9 shows maps of $\log(s_c)$ given different R_p^{local} and $(t_m\sigma_m)$ for each of the three CC configurations, determined by numerical optimization, using Newton's method to guide the search as needed. Fig. 9a is a 3D surface and Fig. 9b is the corresponding contour plot for the 20-μm diameter discrete configuration. The black region of the contour plot indicates where the required s_c is less than the diameter of the CC contact. Fig. 9c and d are contour plots of $\log(s_c)$ corresponding to the parallel and grid configurations, respectively. Note that s_c has units of μm, so for example the contour labeled 3 corresponds to $s_c = 10^3$ μm. The selection criteria R_p^{local} and $(t_m\sigma_m)$ vary over a range of values including those representative of the families of SOFC cathode candidates. The discrete configuration requires smaller s_c than the parallel configuration, which requires a slightly smaller s_c than the grid configuration. This conclusion is in agreement with the potential distribution in Fig. 6.

3.2.2. Large cathodic polarization

At large cathodic polarization, the cell response is a direct, nonlinear function of the nominal global cathodic overpotential, η, and temperature. The critical CC spacing, $s_c^{large\,\eta}$, is smaller than the linear case, $s_c^{small\,\eta}$ of the previous section. This deviation may be expressed as an adjustment factor, a.f.:

$$\text{a.f.} = \frac{s_c^{large\,\eta}}{s_c^{small\,\eta}} \tag{32}$$

Fig. 10 gives a.f. as a function of η and T for the grid and parallel CC configuration cases. The a.f. is independent of R_p^{local} and $(t_m\sigma_m)$, a result that may be shown analytically and is due primarily to the fact that the potential profiles are affected in the same way by varying η and T. Unfortunately, a.f. is not constant in $R_p^{local} - (t_m\sigma_m)$ space when discrete CCs are used because the CC footprint is a different fraction of the active surface area at different values of s_c (see Fig. 2b), which is not a concern for the parallel and grid configurations as modeled. Thus, Fig. 10 does not apply to the discrete configuration.

To use the adjustment factor, $s_c^{small\,\eta}$ corresponding to a combination of R_p and $(t_m\sigma_m)$ may be selected from Fig. 9. Then, to adjust it for larger polarization, a factor is chosen from Fig. 10 based on η and T. Note that if multiple temperatures are to be evaluated, new small polarization R_p^{local} and $(t_m\sigma_m)$ values should likely be used and a new $s_c^{small\,\eta}$ chosen from Fig. 9 for each temperature, since both are typically strong functions of temperature.

3.2.3. Map discussion

These maps may be used to aid design of thin-film test cell geometries for arbitrary MIEC materials under arbitrary test condi-

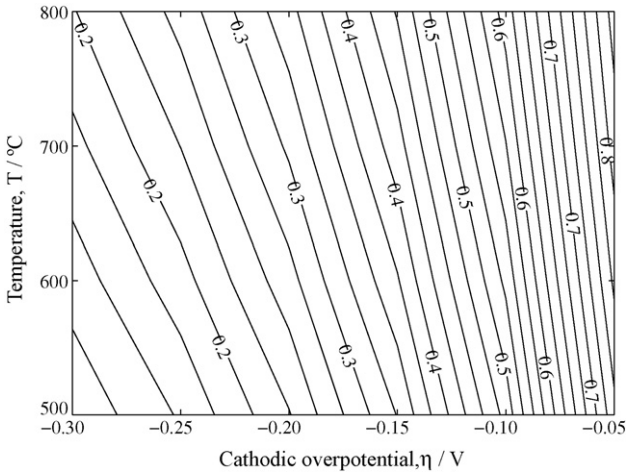

Fig. 10. Contour plots of the adjustment factor to small-η s_c at combinations of η and T (large-polarization model) for the grid and parallel CC configurations, but not valid for the discrete CC configuration. Vanishingly thin electrolyte assumed. The a.f. is valid for any $R_p^{local} - (t_m\sigma_m)$ combination.

tions. At small polarizations, if R_p^{local} and σ_m can be estimated and t_m of the film determined, then the CC spacing required to prevent R_{tot} from exceeding R_{tot}^{ideal} by more than 0.5%, and thus keeping the potential uniform, can be determined from Fig. 9. The s_c value can be determined in principle for large polarization with parallel/grid configuration from Fig. 10 using the a.f. to adjust the small polarization case. Likewise, if the CC configuration must be fixed, the level sets in the contour plots show which combinations of R_p^{local} and $(t_m\sigma_m)$ lead to no more than a 0.5% increase in R_{tot}. Similar maps can be generated for any threshold. If R_p^{local} and σ_m must be estimated and not directly measured, then underestimating both provides a conservative estimate for s_c.

The large-polarization calculations assume BV kinetics and constant σ_m. The extrapolation of linear (small cathodic polarization) kinetics to larger polarization is a less severe estimate and is perhaps more appropriate than the large cathodic polarization calculations if the kinetics of the material being studied are not strictly dominated by charge transfer. The BV kinetics in Fig. 10 are then in some sense illustrative, they show a trend at large polarization but are not as generally applicable as the small polarization treatment in Fig. 9. We recommend that the reader perform similar analysis with material-specific data using the tabular approach described in Section 2.5 at large polarization to provide more accurate estimations for their particular system.

There is no set CC spacing for any specific MIEC or family of MIECs. Generally, the thinner the film, the smaller CC spacing that is required. Even when the thickness is held constant, though, a change to polarization, temperature, partial pressure of oxygen, or electrochemical history can cause a change to R_p^{local} or σ_m that can significantly alter the required CC spacing. CC spacing should be designed based on the planned experimental conditions or possible worst-case scenario for specific materials.

4. Conclusion

In this contribution, an empirical numerical model was presented to simulate potential distribution and current/resistance response under various material and catalytic parameters, CC configurations, cathodic polarizations, and other experimental factors in thin-film, mixed-conducting test cells. Thinner films, larger CC spacings, and thinner electrolytes aggravate sheet resistance, causing the global cell properties such as cell current and cell resistance to vary, sometimes substantially, from the expected value in the case of a well current-collected film. Mitigating sheet resistance with the proper CC spacing is therefore crucial, lest these variations be incorporated into macroscopic experimental results and convoluted with the material's intrinsic catalytic and transport properties.

The model was used to provide guidance for effective CC placement by mapping in parameter space, using local polarization resistance, R_p^{local}, and the product of electrical conductivity and film thickness, $(\sigma_m t_m)$, as selection parameters. In general, continuous crisscrossing metal lines, deposited through e.g. photolithography, provide the best intra-film current collection while small, regularly spaced discrete contacts, provided by e.g. a metal mesh, provide the least efficient intra-film current collection. Most thin-film aspect ratios and CC configurations can be accommodated without severe intra-film sheet resistance provided the CCs are spaced appropriately. With well-designed CCs, a maximum amount of surface area is free to use for other in situ characterization methods such as Raman spectroscopy while ensuring that EIS measurements reflect the true intrinsic properties of the material being studied.

Acknowledgments

The authors thank Lei Yang for supplying the example LSCF film measurements appearing in Table 1, Xiaoyuan Lou and Songho Choi for fabricating the patterned test cell appearing in Fig. 1b, and Professor Yingjie Liu for helpful discussion. This work was supported by the US DOE SECA Core Technology Program under Grant No. DE-NT-0006557.

References

[1] Y. Takeda, R. Kanno, M. Noda, Y. Tomida, O. Yamamoto, J. Electrochem. Soc. 134 (11) (1987) 2656–2661.
[2] O. Yamamoto, Y. Takeda, R. Kanno, M. Noda, Solid State Ionics 22 (2–3) (1987) 241–246.
[3] J. Mizusaki, T. Saito, H. Tagawa, J. Electrochem. Soc. 143 (10) (1996) 3065–3073.
[4] A. Endo, M. Ihara, H. Komiyama, K. Yamada, Solid State Ionics 86–88 (1996) 1191–1195.
[5] K. Masuda, A. Kaimai, K.-i. Kawamura, Y. Nigara, T. Kawada, J. Mizusaki, H. Yugamni, H. Arashi, in: U. Stimming, S.C. Singhal, H. Tagawa, W. Lehnert (Eds.), Solid Oxide Fuel Cells V, vol. PV 97-40, The Electrochemical Society Proceedings Series, 1997, pp. 473–482.
[6] T. Ioroi, T. Hara, Y. Uchimoto, Z. Ogumi, Z. Takehara, J. Electrochem. Soc. 144 (4) (1997) 1362–1370.
[7] T. Ioroi, T. Hara, Y. Uchimoto, Z. Ogumi, Z-i. Takehara, J. Electrochem. Soc. 145 (6) (1998) 1999–2004.
[8] A. Endo, S. Wada, C.J. Wen, H. Komiyama, K. Yamada, J. Electrochem. Soc. 145 (3) (1998) L35–L37.
[9] T. Kawada, K. Masuda, J. Suzuki, A. Kaimai, K. Kawamura, Y. Nigara, J. Mizusaki, H. Yugami, H. Arashi, N. Sakai, H. Yokokawa, Solid State Ionics 121 (1999) 271–279.
[10] A. Endo, H. Fukunaga, C. Wen, K. Yamada, Solid State Ionics 135 (1–4) (2000) 353–358.
[11] C. Mims, N. Joos, P. van der Heide, A. Jacobson, C. Chen, C. Chu, B. Kim, S. Perry, Electrochem. Solid-State Lett. 3 (1) (2000) 59–61.
[12] V. Brichzin, J. Fleig, H.U. Habermeier, J. Maier, Electrochem. Solid-State Lett. 3 (9) (2000) 403–406.
[13] Y. Yang, C. Chen, S. Chen, C. Chu, A. Jacobson, J. Electrochem. Soc. 147 (11) (2000) 4001–4007.
[14] Y.L. Yang, A. Jacobson, C. Chen, G. Luo, K. Ross, C. Chu, Appl. Phys. Lett. 79 (6) (2001) 776–778.
[15] A. Ringuedé, J. Fouletier, Solid State Ionics 139 (3–4) (2001) 167–177.
[16] V. Brichzin, J. Fleig, H.-U. Habermeier, G. Cristiani, J. Maier, Solid State Ionics 152–153 (2002) 499–507.
[17] T. Kawada, J. Suzuki, M. Sase, A. Kaimai, K. Yashiro, Y. Nigara, J. Mizusaki, K. Kawamura, H. Yugami, J. Electrochem. Soc. 149 (7) (2002) E252–E259.
[18] N. Imanishi, T. Matsumura, Y. Sumiya, K. Yoshimura, A. Hirano, Y. Takeda, D. Mori, R. Kanno, Solid State Ionics 174 (2004) 245.
[19] F.S. Baumann, J. Fleig, M. Konuma, U. Starke, H.-U. Habermeier, J. Maier, J. Electrochem. Soc. 152 (10) (2005) A2074.
[20] E. Koep, C. Compson, M.L. Liu, Z.P. Zhou, Solid State Ionics 176 (1–2) (2005) 1–8.
[21] E. Koep, D.S. Mebane, R. Das, C. Compson, M. Liu, Electrochem. Solid-State Lett. 8 (11) (2005) A592–A595.
[22] R. Radhakrishnan, A.V. Virkar, S.C. Singhal, J. Electrochem. Soc. 152 (1) (2005) A210–A218.

[23] F.S. Baumann, J. Fleig, H.-U. Habermeier, J. Maier, Solid State Ionics 177 (2006) 1071–1081.
[24] D. Mori, H. Oka, Y. Suzuki, N. Sonoyama, A. Yamada, R. Kanno, Y. Sumiya, N. Imanishi, Y. Takeda, Solid State Ionics 177 (2006) 535–540.
[25] G.J. la O', B. Yildiz, S. McEuen, Y. Shao-Horn, J. Electrochem. Soc. 154 (4) (2007) B427–B438.
[26] M. Prestat, A. Infortuna, S. Korrodi, S. Rey-Mermet, P. Muralt, L.J. Gauckler, J. Electroceram. 18 (1–2) (2007) 111–120.
[27] T.T. Fister, D.D. Fong, J.A. Eastman, P.M. Baldo, M.J. Highland, P.H. Fuoss, K.R. Balasubramaniam, J.C. Meador, P.A. Salvador, Appl. Phys. Lett. 93 (15) (2008) 151904.
[28] D.S. Mebane, Y. Liu, M. Liu, J. Electrochem. Soc. 154 (5) (2007) A421–A426.
[29] M.E. Lynch, D.S. Mebane, Y. Liu, M. Liu, J. Electrochem. Soc. 155 (6) (2008) B635–B643.
[30] J. Fleig, F.S. Baumann, V. Brichzin, H.R. Kim, J. Jamnik, G. Cristiani, H.U. Habermeier, J. Maier, Fuel Cells 6 (3–4) (2006) 284–292.
[31] S.B. Adler, J. Electrochem. Soc. 149 (5) (2002) E166–E172.
[32] J. Winkler, P.V. Hendriksen, N. Bonanos, M. Mogensen, J. Electrochem. Soc. 145 (4) (1998) 1184–1192.
[33] G. Reinhardt, W. Gopel, in: T. Ramanarayanan, W. Worrell, H. Tuller, M. Mogensen, A. Khandkar (Eds.), Ionic and Mixed Conducting Ceramics III, vol. PV 97-24, The Electrochemical Society Proceedings Series, 1998, pp. 610–630.
[34] R.I. Tucceri, D. Posadas, J. Electrochem. Soc. 128 (7) (1981) 1478–1483.
[35] R.G. Keil, J. Electrochem. Soc. 133 (7) (1986) 1375–1379.
[36] T.O. Drews, S. Krishnan, J.C. Alameda, D. Gannon, R.D. Braatz, R.C. Alkire, IBM J. Res. Dev. 49 (1) (2005) 49–63.
[37] J. Fleig, J. Maier, Electrochim. Acta 41 (7–8) (1996) 1003–1009.
[38] M.H.R. Lankhorst, H.J.M. Bouwmeester, H. Verweij, Solid State Ionics 96 (1–2) (1997) 21–27.
[39] J. Mizusaki, Y. Yonemura, H. Kamata, K. Ohyama, N. Mori, H. Takai, H. Tagawa, M. Dokiya, K. Naraya, T. Sasamoto, H. Inaba, T. Hashimoto, Solid State Ionics 132 (3–4) (2000) 167–180.
[40] J. Mizusaki, T. Sasamoto, W.R. Cannon, H.K. Bowen, J. Am. Ceram. Soc. 66 (4) (1983) 247–252.
[41] J. Mizusaki, M. Yoshihiro, S. Yamauchi, K. Fueki, J. Solid State Chem. 58 (2) (1985) 257–266.
[42] J. Newman, K. Thomas-Alyea, Electrochemical Systems, third ed., Wiley-Interscience, Hoboken, NJ, 2004.
[43] J. Jamnik, J. Maier, Phys. Chem. Chem. Phys. 3 (9) (2001) 1668–1678.
[44] W. Sitte, E. Bucher, A. Benisek, W. Preis, Spectrochim. Acta, Part A 57 (10) (2001) 2071–2076.
[45] J. Mizusaki, J. Tabuchi, T. Matsuura, S. Yamauchi, K. Fueki, J. Electrochem. Soc. 136 (7) (1989) 2082–2088.
[46] H.U. Anderson, C.-C. Chen, L.-W. Tai, M.M. Nasrallah, in: T.A. Ramanarayanan, W.L. Worrell, H.L. Tuller (Eds.), Ionic and Mixed Conducting Ceramics (Second International Symposium), vol. PV 94-12, The Electrochemical Society Proceedings Series, 1994, pp. 376–387.
[47] M.H.R. Lankhorst, J.E. ten Elshof, J. Solid State Chem. 130 (2) (1997) 302–310.
[48] S.R. Wang, M. Katsuki, M. Dokiya, T. Hashimoto, Solid State Ionics 159 (1–2) (2003) 71–78.
[49] V.M.W. Huang, V. Vivier, M.E. Orazem, N. Pebere, B. Tribollet, J. Electrochem. Soc. 154 (2) (2007) C99–C107.
[50] M.E. Orazem, B. Tribollet, Electrochemical Impedance Spectroscopy, Wiley, Hoboken, NJ, 2008.
[51] J.O. Bockris, A. Reddy, M. Gamboa-Aldeco, Modern Electrochemistry 2A: Fundamentals of Electrodics, second ed., Kluwer Academic/Plenum Publishers, New York, 2000.
[52] D.S. Mebane, M. Liu, J. Solid State Electrochem. 10 (2006) 575–580.
[53] J. Mizusaki, Solid State Ionics 52 (1–3) (1992) 79–91.
[54] M.F. Ashby, Materials Selection in Mechanical Design, second ed., Butterworth-Heinemann, Oxford, UK, 1999.
[55] L.W. Tai, M.M. Nasrallah, H.U. Anderson, D.M. Sparlin, S.R. Sehlin, Solid State Ionics 76 (3/4) (1995) 273–283.